

Diffusion distinguishes between structural universality classes of disordered media

Antonios Papaioannou,¹ Dmitry S. Novikov,² Els Fieremans,² and Gregory S. Boutis^{1,3}

¹City University of New York, The Graduate Center, Department of Physics, New York, NY, USA

²Center for Biomedical Imaging, Department of Radiology,
New York University School of Medicine, New York, NY, USA

³City University of New York, Brooklyn College, Department of Physics, Brooklyn, NY, USA

(Dated: February 21, 2022)

Identifying relevant parameters is central to understanding complex phenomena. This often evokes the concept of universality, which groups microscopically distinct systems into a handful of universality classes, according to the relevant degrees of freedom affecting their thermodynamic and dynamical properties. Here we show that universality is key to relating transport to structure in disordered systems. We experimentally demonstrate the relation between the structural exponent, characterizing a structural universality class, and the dynamical exponent of classical diffusion in disordered media. To that end, we manufactured samples of hyperuniform and short-range disorder, characterized by the statistics of the placement of μm -thin parallel barriers permeable to water. We used NMR-measured water diffusion to identify the structural universality class of these samples via the dynamical exponent describing the power-law decrease of the diffusion coefficient across the barriers at long times. Our experimentally established relation between structure and transport exemplifies the hierarchical nature of structural complexity: dynamics is mainly determined by the universality class, whereas microscopic parameters affect the non-universal coefficients. Our results open the way for non-invasive characterization of structural correlations in porous media, complex materials, and biological tissues via a bulk diffusion measurement.

How does a macroscopic measurement relate to microscopic structure? This ill-posed question has been repeatedly asked in many disciplines — famously, “Can one hear the shape of a drum?” [1] — and its answer depends on the kind of the measurement. Naively, one could imagine that infinitely many parameters, needed to specify sample’s structure, would in one way or the other contribute to the outcome. Physical intuition, however, tells that only a few parameters profoundly affect the measurement; identifying these relevant parameters is generally nontrivial, especially for irregular, or *disordered* systems. For instance, even small irregularities in a periodic lattice can change perfectly conducting metallic bands into an insulator due to quantum localization [2].

Here we consider classical diffusion in a structurally disordered system, where the practical answer to the above question could help quantify the underlying microstructure of materials [3–6] and living tissues [7–11]. We experimentally demonstrate that the qualitative behavior of the time-dependent diffusion coefficient is tied to the long-range structural fluctuations. While systems may strongly differ in their microscopic parameters, there are only a few *universality classes* of such fluctuations — in essence, a system can be disordered in one of a few distinct ways — and each universality class yields a particular power-law behavior of the observed macroscopic diffusion coefficient.

Technically, we experimentally verify the general relation [8]

$$\vartheta = \frac{p + d}{2}, \quad (1)$$

between the structural exponent p , and the dynamical exponent ϑ of the Brownian motion x_t in structurally disordered stationary media in d spatial dimensions. The defining signature of structural complexity is reflected in the structural ex-

ponent p which takes discrete values according to the universality class, as illustrated in Fig. 1 for our $d = 1$ -dimensional samples. Equation (1) relates p to the long-time tail in the bulk diffusion coefficient [8] (the mean-squared displacement rate)

$$D_{\text{inst}}(t) \equiv \frac{\partial}{\partial t} \frac{\langle (x_t - x_0)^2 \rangle}{2} \simeq D_\infty + c \cdot t^{-\vartheta}, \quad t \rightarrow \infty. \quad (2)$$

The macroscopic diffusion coefficient $D_\infty \equiv D_{\text{inst}}(t)|_{t=\infty}$ and the power-law amplitude c are non-universal, i.e. depend on the microstructural parameters. On the other hand, as we experimentally demonstrate in Fig. 2, the relation (1) is universal [8], akin to the relations between critical exponents [12] in statistical physics, where the notion of universality originates.

Formally, the structural universality class is defined [8] by the $k \rightarrow 0$ scaling of the power spectrum

$$\Gamma(k) \equiv \int_V d\mathbf{r} e^{-i\mathbf{k}\mathbf{r}} \langle n(\mathbf{r}_0 + \mathbf{r}) n(\mathbf{r}_0) \rangle_{\mathbf{r}_0} = \frac{|n(\mathbf{k})|^2}{V} \sim k^p \quad (3)$$

of the restrictions which embody the sample’s microscopic structure. The exponent p , taking a handful of discrete values such as in Fig. 1e, describes how fast the spatial correlations $\Gamma(\mathbf{r})$ in the density of the restrictions $n(\mathbf{r})$ decay at large distances r , and thereby characterizes the system’s heterogeneity. The values $p > 0$ correspond to *hyperuniform* media [13, 14] (sample C), where the fluctuations are suppressed relative to the short-range (Poissonian) disorder ($p = 0$, samples A and B); $p < 0$ correspond to *strong disorder*, where the fluctuations are enhanced [7, 8]. Qualitatively, the variance in the number of restrictions within a volume V grows $\propto V$ for short-range disorder (according to the central limit theorem), slower than V for hyperuniform disorder (such as in maximally random jammed packings [15]), and faster than

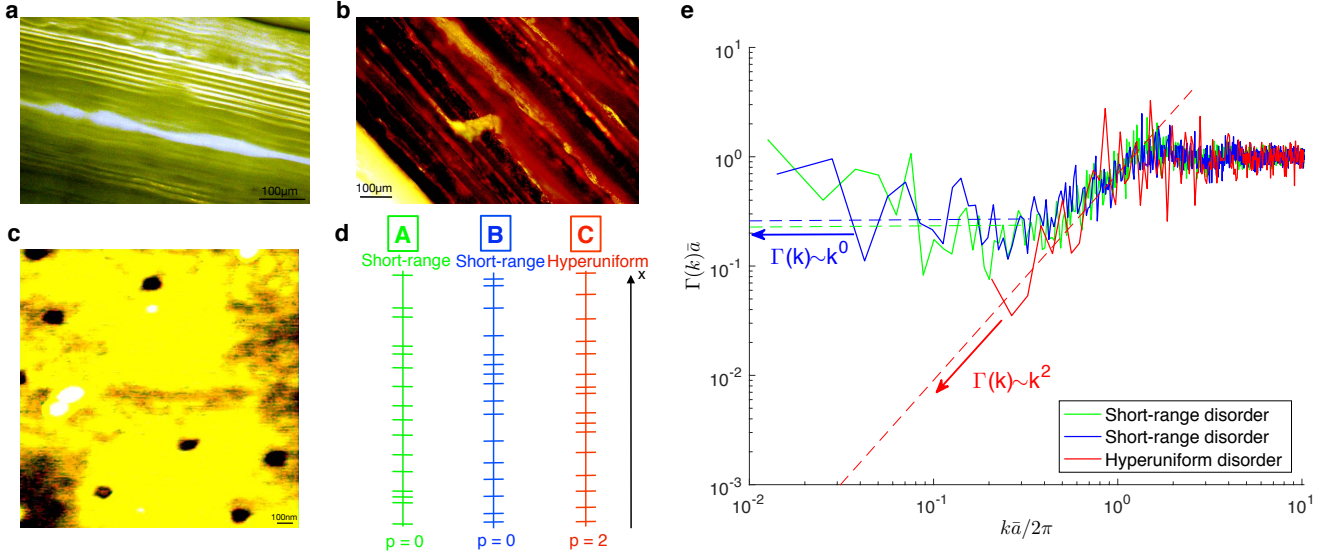


FIG. 1. Structure and universality classes of the samples. Representative optical microscopy image of the SR sample, **a**, and of the HU sample, **b**, made of parallel, permeable barriers. Rectangular copper plates were inserted to achieve hyperuniformity (see Methods and supplementary Fig. S1). **c**, AFM image of a representative nanoporous polycarbonate barriers. **d**, Digitized 1d cut-outs of the samples from **a** and **b**: two different realizations of SR disorder in $n(x)$ using barriers with different permeability (A-B), and HU sample (C). Water diffusion (2) was measured transverse to the barriers with NMR [3], Fig. 2. **e**, Power spectrum (3) of the film density $n(x)$ reveals qualitative differences between the disorder classes as $k \rightarrow 0$: A plateau ($p = 0$) in $\Gamma(k)$ for the SR samples (samples A and B), and k^p scaling with $p = 2$ for HU sample (sample C). These differences are not evident from the local cut-outs in **d**, as they characterize global structural organization.

V for strong disorder. The relation (1) relies on self-averaging [16], $p + d > 0$, ensuring the existence [8] of finite D_∞ .

Two samples exhibiting short-range (SR) disorder were constructed by stacking flat permeable barriers (porous films) in a glass tube filled with H_2O (cf. Methods section). A digitized cut-out of the samples is shown in Fig. 1d (samples A-B) corresponding to two different realizations of short-range disorder. A representative optical microscopy image, Fig. 1a, yields an average spacing $\bar{a} \approx 12.5 \mu\text{m}$ between the centers of the barriers. The experimentally determined power spectra (3) for both samples, shown in Fig. 1e, exhibit a finite plateau $\Gamma(k) \sim k^0$, as $k \rightarrow 0$, corresponding to the structural exponent $p = 0$ and verify the expected short-range disorder.

On the other hand, the hyperuniform (HU) disordered sample C, shown in Fig. 1d, is characterized by reduced long-range structural fluctuations, achieved by placing identical rectangular copper plates between the permeable barriers (cf. Methods section and Supplementary materials Fig. S1). Ideally, the barriers would create a periodic lattice (with $\bar{a} \approx 62.0 \mu\text{m}$) which would result in Bragg peaks in $\Gamma(k)$ and $\Gamma(k < \pi/\bar{a}) \equiv 0$. However, experimental inaccuracies in the placement of the barriers and copper plates act as random displacements from ideal lattice positions, resulting in apparent hyperuniformity [13] of a “shuffled lattice” kind [17], for which the power spectrum $\Gamma(k) \sim k^2$ for $k\bar{a} \ll 1$. The spectrum in Fig. 1e is indeed consistent with the exponent value $p = 2$.

We underscore that it is practically impossible to discern the qualitative differences between the samples A, B and C — or to reveal the disorder universality class by the naked eye.

Based on local sample cut-outs, shown in Fig. 1d, the three samples look very similar, when the dimensions are rescaled such that mean barrier spacing is the same for all of them. However the power spectrum $\Gamma(k)$, shown in Fig. 1e, readily shows similarity between samples A and B, and their qualitative difference from sample C, as its low k scaling captures the universal features in the large-scale behavior of the density fluctuations. In what follows, we show how a bulk diffusion measurement distinguishes between the SR and HU classes, thereby yielding the form of $\Gamma(k)$ for $k\bar{a} \ll 1$ (i.e. for distances exceeding \bar{a}), and experimentally validating the relation (1) in dimension $d = 1$.

For that, the conventional cumulative $D(t) \equiv \langle (x_t - x_0)^2 \rangle / 2t$ of H_2O was measured using pulse-gradient diffusion NMR [3] over a broad range of diffusion times t , from 1.0 ms to 4.5 s, spanning over 3 orders of magnitude, and translating to mean square displacements $\langle (x_t - x_0)^2 \rangle^{1/2}$ ranging from $2 \mu\text{m}$ to $144 \mu\text{m}$. Measuring such short mean square displacements requires fast switching and strong in magnitude, gradient pulses. Therefore a homemade gradient coil was constructed [18, 19] capable of delivering gradient pulses of approximately 90 G/cmA. However, such strong gradient pulses may introduce experimental errors in the experimental data, such as those due to eddy currents. To mitigate such effects, two pulse sequences were used for the diffusion measurements (cf. Methods and Supplementary Materials) which made use of bipolar gradient pulses for short times, and asymmetric pulses for long times.

Figure 2a shows the time dependence of the cumulative diffusion coefficient $D(t)$, of H_2O diffusing through the three

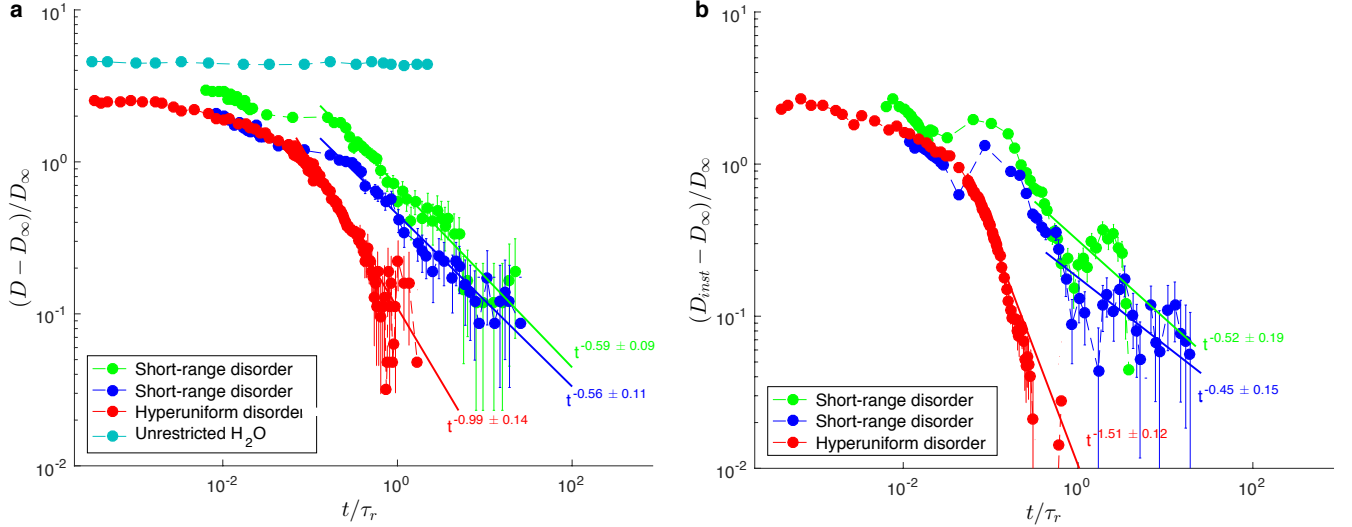


FIG. 2. Dynamical exponent (1) identifies the disorder classes. **a**, The tail in the cumulative diffusion coefficient $D(t)$ (see text) distinguishes between SR and HU disorder, via exponent $\tilde{\vartheta} = \min\{\vartheta, 1\}$ (Table I). Note that $\tilde{\vartheta} \equiv \vartheta \approx 1/2$ for both SR samples (made of barriers with different permeability), while $\tilde{\vartheta} \approx 1$ for the HU sample, indicating that the “true” $\vartheta > 1$. $D(t) = \text{const}$ for unrestricted water is shown for comparison. **b**, To access ϑ for HU disorder, we obtain the tail in $D_{\text{inst}}(t)$, equation (2). While results are noisier due to numerical differentiation, the exponent values $\vartheta \approx 1/2$ for SR and $\vartheta \approx 3/2$ for HU, cf. Table I, are consistent with equation (1).

samples, as well as for unrestricted H_2O (cyan). While there is no time dependence in $D(t)$ for unrestricted H_2O , a power-law exponent $\tilde{\vartheta} = 0.59 \pm 0.09$ in $D(t) - D_\infty \sim t^{-\tilde{\vartheta}}$ was observed for H_2O diffusing through sample A and $\tilde{\vartheta} = 0.56 \pm 0.11$ for sample B. The exponents are in remarkable agreement with equation (1) for $p = 0$ and $d = 1$, and with earlier prediction [20] for the tail in $D(t)$ for Poissonian statistics of restrictions. On the other hand $D(t) - D_\infty$ for H_2O diffusing through the HU sample exhibits the $1/t$ tail with $\tilde{\vartheta} = 0.99 \pm 0.14$. The structural and dynamical exponents, as well as main characteristic of the samples, such as residence and diffusion times τ_r and τ_D , are given in Table I.

The $1/t$ tail in $D(t)$ in the HU sample indicates that $\vartheta > 1$. Indeed, the cumulative $D(t) \equiv \frac{1}{t} \int_0^t d\tau D_{\text{inst}}(\tau)$ may be used to determine ϑ only in the case when the power-law tail in $D_{\text{inst}}(t)$ is sufficiently slow, [8] $\vartheta < 1$. In this case, the instantaneous mean squared displacement rate (2) has similar behavior to the average rate $\langle (x_t - x_0)^2 \rangle / 2t$ over the whole interval t ; formally, the above integral converges at the upper limit. However, when the underlying $\vartheta > 1$, the tail $D(t) - D_\infty = \frac{1}{t} \int_0^t d\tau [D_{\text{inst}}(\tau) - D_\infty] \simeq \frac{1}{t} \int_0^\infty d\tau [D_{\text{inst}}(\tau) - D_\infty]$ is determined by the short τ , such that the $1/t$ factor overshadows the effect of ϑ . In other words, $D(t) - D_\infty \sim t^{-\tilde{\vartheta}}$, where $\tilde{\vartheta} = \min\{\vartheta, 1\}$. Hence, if the tail in $D(t)$ has $\tilde{\vartheta} = 1$, which is the case for the HU sample, one has to obtain $D_{\text{inst}}(t)$ via numerical differentiation to uncover the true $\vartheta > 1$, with the expense of amplifying the experimental noise.

Figure 2b shows the computed instantaneous $D_{\text{inst}}(t) = \partial_t [tD(t)]$, using numerical differentiation with Savitzky-Golay (SG) regularization [21] (cf. Methods). As expected, for both SR samples, $D_{\text{inst}}(t)$ reaches its universal limit D_∞

according to equation (2) with $\vartheta = 0.52 \pm 0.19$ for sample A and $\vartheta = 0.45 \pm 0.15$ for sample B (cf. Table I), consistent with the above results for $\tilde{\vartheta}$ and equation (1) with $p = 0$ and $d = 1$. For the HU sample, the dynamical exponent $\vartheta = 1.51 \pm 0.12$, is notably different from that for SR samples, and in agreement with equation (1) for $p = 2$ and $d = 1$. Least squares fit was stable with respect to SG filtering window and polynomial order, with reasonable values $\chi^2/\text{dof} \approx 2$ (cf. Supplementary Materials for details, Fig. S4-S5).

To put our results into context, previous applications of bulk diffusion for characterizing microstructure below imaging resolution focussed on the *short-time* [22] initial decrease $D(t) \simeq D_0(1 - \frac{4\sqrt{D_0}}{3d\sqrt{\pi}} \frac{S}{V} \cdot t^{1/2})$ of the cumulative diffusion coefficient, as a result of the increasing fraction $\sim \sqrt{D_0 t} S/V$ of random walkers restricted by walls. In this limit, it is the *net amount* of the restrictions that is relevant, irrespective of their positions in space — akin to the net drum surface area derived from the density of high frequency eigenmodes [1]. This technique has been used for quantifying the surface-to-volume ratio (S/V) of porous media [4] and biological samples such as red blood cell suspensions [23] and brain tumor cells in mice [24].

Experimentally, the short-time limit is highly demanding on the pulsed field gradients. Hence, it has not become widespread in *in-vivo* MRI [11]. However, for our samples, displacements as short as $L(t) \approx 2 \mu\text{m}$ are accessible with our homemade gradient coil. Fig. 3 highlights the initial $t^{1/2}$ decrease of $D(t)$ for $t/\tau_D \ll 1$, when the short time limit is valid (cf. Table I for the values of τ_D). For sample A, the average spacing of the barriers was determined from $S/V \equiv 2/\bar{a}$, and found to be $\bar{a} = 11.4 \mu\text{m}$, deviating by $\sim 9\%$ from

| Sample | Disorder class | p | $\tilde{\vartheta}_{\text{th}}$ | $\tilde{\vartheta}$ | ϑ_{th} | ϑ | τ_r , ms | τ_D , ms | D_∞ , $\frac{\mu\text{m}^2}{\text{ms}}$ | \bar{a} , μm | Pore diam., nm |
|-----------|----------------|-----|---------------------------------|---------------------|-------------------------|-----------------|---------------|---------------|--|---------------------------|----------------|
| A (green) | SR | 0 | 1/2 | 0.59 ± 0.09 | 1/2 | 0.52 ± 0.19 | 157.2 | 34.2 | 0.42 ± 0.04 | 12.5 | 15 |
| B (blue) | SR | 0 | 1/2 | 0.56 ± 0.11 | 1/2 | 0.45 ± 0.15 | 117.2 | 43.0 | 0.58 ± 0.05 | 14.1 | 45 |
| C (red) | HU | 2 | 1 | 0.99 ± 0.14 | 3/2 | 1.51 ± 0.12 | 2949.0 | 754.9 | 0.63 ± 0.04 | 58.9 | 45 |

TABLE I. Sample parameters and exponents for disorder classes. Theoretical and experimental power-law exponents $\tilde{\vartheta}$ and ϑ in the tails of $D(t)$ and $D_{\text{inst}}(t)$ determined from Fig. 2. Note that the theoretical value ϑ_{th} is calculated according to equation (1). Shown also are the (non-universal) macroscopic diffusion coefficient, D_∞ , mean barrier spacing \bar{a} , pore diameter of the barriers, residence time $\tau_r \equiv \bar{a}/2\kappa$, and time to diffuse in-between barriers, $\tau_D \equiv \bar{a}^2/2D_0$.

the value expected from the images acquired via optical microscopy. Similarly, for sample A the average spacing obtained from the short-time limit was $\bar{a} = 12.0 \mu\text{m}$, deviating by $\sim 15\%$ from the value expected from the images acquired via optical microscopy. For HU sample, $\bar{a} = 61.5 \mu\text{m}$ deviated by approximately $\sim 4\%$ from the predicted value. In the least squares fits shown in Fig. 3, the free diffusion coefficient D_0 was fixed to the exact value at the corresponding temperature. In Supplementary Materials (Fig. S6), we discuss effects of fixing/releasing D_0 and varying the time window of the fit, by performing statistical analysis for the dof = 1 and 2.

As mentioned earlier, the initial $t^{1/2}$ decrease, sensitive only to the net amount of restrictions, cannot reveal structural correlations. Therefore, the qualitative differences between the two disorder classes are not apparent in Fig. 3 — only the quantitative differences in $S/V = 2/\bar{a}$ are seen in the slopes of the curves at small t . Similarly, the non-universal coefficient c and the tortuosity limit D_∞ in equation (2) reflect the density of the barriers and their permeability (cf. Supplementary Materials, section), but cannot reveal the qualitative differences in the long-range fluctuations in barrier positions.

To summarize, our experiments for the first time reveal the qualitative difference in the diffusive dynamics between sam-

ples with qualitatively different spatial statistics of structural fluctuations, justifying the application of the concept of universality to classical transport in disordered media, and validating the fundamental relation (1) between structural and dynamical exponents. The coefficients c and D_∞ of equation (2) for the two SR samples are non-universal, depending on microscopic parameters of the barriers. However, the dynamical exponent ϑ remains the same, because the statistics of large-scale fluctuations for both samples A and B are governed by the Central limit theorem (finite correlation length, a plateau in $\Gamma(k)|_{k \rightarrow 0}$). On the other hand, based on the dynamical exponent ϑ , qualitative differences were revealed between the samples exhibiting short-range (A, B), and hyperuniform disorder (C) (where fluctuations are reduced [13, 14] relative to those governed by Central limit theorem since $\Gamma(k)|_{k \rightarrow 0} \rightarrow 0$), verifying that diffusion can identify the structural universality class of the medium.

After the seminal 1991 observation of diffusion diffraction [25] yielding the structure factor of water-filled identical confining pores, the late Paul T. Callaghan insightfully referred to diffusion as microscopy [3]. This q -space technique has enabled determination of the shape of regular confining structures with impermeable walls, such as pores of similar shape [26]. The present investigation suggests that the time-dependent diffusion coefficient (2) reveals the parameter that microscopy does not provide — the elusive to the naked eye statistics of structural correlations, which are able to distinguish and characterize randomly looking, or *disordered*, and *permeable* samples such as those in Fig. 1c, from a low-resolution bulk transport measurement. As most building blocks of living tissues, such as cells and organelles, are not fully confining (cells have permeable walls; water can move along the dendrites and axons), we believe this fundamental result can serve as a basis for quantitative investigations of μm -level structural correlations in complex materials [6] and in live biological tissues [7–10] with diffusion NMR and MRI.

Methods

Sample construction. Two sets of commercial porous polycarbonate films (barriers) were purchased from Sterlitech Corporation (Kent, WA). The pore diameters were 15 nm (sample A in Fig. 1d) and 45 nm (sample B-C in Fig. 1d). The films had a thickness of approximately $6 \mu\text{m}$, and pore density of approximately 8 pores/ μm^2 as revealed via Atomic Force Microscopy shown in Fig. 1c.

Short-range disorder (A,B)—The polycarbonate films were cut in rectangular pieces of 0.95 mm in width and 7 mm in length with a

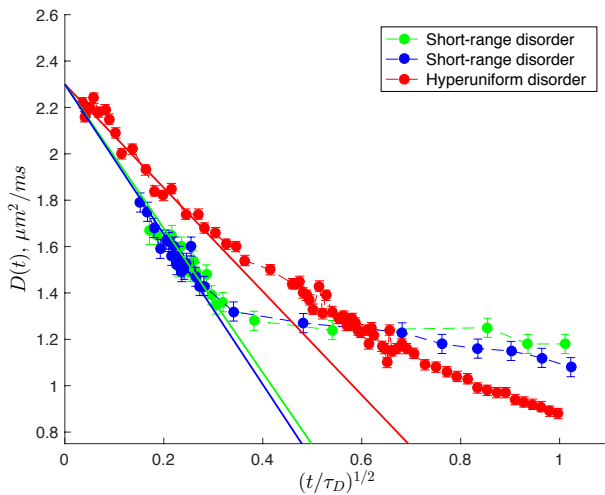


FIG. 3. Short time $t^{1/2}$ decrease [22] of $D(t)$: Quantifying the net amount of restrictions, $S/V = 2/\bar{a}$; the difference in the large scale fluctuations is not revealed. The cumulative diffusion coefficient $D(t)$ exhibits the $t^{1/2}$ decrease for $t/\tau_D \ll 1$.

scalpel and stacked in a layered geometry along the x axis by hand using tweezers, as shown in Fig. 1d. The films were then placed in a rectangular NMR glass tube purchased from F&D Glass (Millville, NJ) (1 mm in height, 1 mm in width, 9 mm in length), filled with water and sonicated for 3 minutes. The samples were inspected under a microscope to avoid bubbles which may distort the RF and gradient fields. Two SR samples were constructed: one using the films with 15 nm pore diameter (A in Fig. 1) and one using the films with 45 nm pore diameter (B in Fig. 1). SR samples had 86–87 films stacked along x resulting in a predicted $\bar{a} \simeq 12 \mu\text{m}$. A representative optical microscopy image of the SR sample B created with the 45 nm pore diameter films is shown in Fig. 1a.

Hyperuniform disorder (C)—The same set of 45 nm pore diameter polycarbonate permeable films was used to create the sample exhibiting hyperuniform disorder. In addition to the films, a customized set of spacers was used to achieve a semi-periodic geometry. The spacers were designed in the lab using Google Sketchup and built by Micron Solutions LLC (Salt Lake City, UT); the spacers had a length of 7 mm, 0.95 mm width, and a thickness of 45 μm . The thickness of the films was chosen so that the experimental errors in the placement of the films act as random drifts resulting in hyperuniformity (see main text) [13]. The spacers were made of copper and designed with an open end to minimize eddy currents. The resulting sample was made by placing the films and spacers in an alternating fashion (cf. Supplementary Materials Fig. S1). An optical microscopy image of the sample is shown in Fig. 1b.

Diffusion NMR. All experiments were performed on a 4.2 Tesla Tecmag Apollo system using a homemade probe equipped with high magnetic field gradients [18, 19]. The gradient coil was composed of two Maxwell pairs of 44 and 6 loops and had a diameter of 8 mm. The gradient set was capable of delivering magnetic field gradients of approximately 90 G/cm/Amp along the “ z ” direction (of the main magnetic field). Gradient was aligned in the direction normal to the surface of the permeable barriers (shown as x in the main text for the sake of more general notation). The temperature was set to 25°C and was regulated to within 0.5°C; at this temperature the theoretical diffusion coefficient is $D_0 = 2.30 \mu\text{m}^2/\text{ms}$ [27]. Sample heating due to the application of high magnetic field gradients was tested based on chemical shift temperature measurements in methanol [28]; temperature variations were found to be less than 2% (°C).

The applied magnetic field gradients g_m ranged from approximately 5 G/cm to 1,000 G/cm and were calibrated using the theoretical diffusion coefficient at 25°C. Two pulse sequences were used for measuring the diffusion coefficient. For diffusion times, t , between 1 ms to 50 ms the pulse sequence is shown in Supplementary Fig. S2a [29]. For t between 50 ms – 4.5 s the sequence is shown in Supplementary Fig. S2b [30, 31]. The gradient pulse width δ ranged between 120–240 μs . The diffusion time t is defined in terms of sequence timings in the Supplementary Materials. For the diffusion measurements, the number of averages ranged from 160–700 resulting in total time of approximately 2 weeks for acquiring a single $D(t)$ curve (i.e. for one sample).

There are four basic causes that artificially lower the measured diffusion coefficient: eddy currents, magnetic field inhomogeneities, surface relaxation, and higher order terms in the cumulant expansion [32]. Sinusoidal pulses were used to mitigate ring-down effects which may result in slight errors in the q -space trajectory [33]. In addition, π pulses were used to refocus evolution under the background field gradients at time 4τ . The surface relaxation was also found to be minimal due to the relatively long spin-lattice relaxation times of H_2O imbedded in the polycarbonate films ($T_1 \simeq 1.8$ s). Lastly, higher order cumulants were suppressed by keeping the product $bD_0 < 1$ so that $\ln S \simeq -bD_0$ for all diffusion times probed in this work. The diffusion weighting parameter $b \sim (g_m\delta)^2 t$ was

fixed to $b = 0.40 \text{ ms}/\mu\text{m}^2$ (see Supplementary Materials for precise definition of b in terms of sequence parameters).

Short-time regime—For the short time measurements ($t = 1$ ms to 50 ms), bipolar gradients were used to mitigate eddy currents induced by the fast changing current in the gradient coils. It should be noted that the sinusoidal shaped gradient pulses alternate the form of b given in ref. [29]; the derivation of the b value for sinusoidal shaped gradient pulses is given in Supplementary Materials.

Long-time regime—For the long time measurements (50 ms to 4.5 s), applying a fixed b -value requires reducing the applied gradient g_m , such that it may become comparable with susceptibility-induced background gradients g_0 which may alter the q -space trajectory. Asymmetric pulses were used to mitigate the cross-term proportional to $g_0 g_m$ in the cumulant expansion during both encoding and decoding periods. Due to the sinusoidal shaped gradient pulses, we recalculated the expression for the b -value as compared to refs. [30, 31].

Numerical differentiation. The computation of D_{inst} reported in Fig. 2c requires taking the derivative of the measured cumulative diffusion coefficient as $D_{\text{inst}}(t) = \partial_t[tD(t)]$. This operation amplifies experimental noise and therefore a Savitzky-Golay (SG) filter with a dynamical window that increases with respect to time was implemented [21]. The minimum SG window size and polynomial order were chosen such that χ^2/dof and error ϵ_ϑ in ϑ is minimal. We chose a filter with polynomial order 2, and a filtering window of $\pm 60\%$ of the central time point on the fitting polynomial. A least squares fit with $\text{dof} = 2$ was used for ϑ and c by fixing the D_∞ value to that from the $D(t)$ fit at long t . The resulting $\chi^2/\text{dof} \approx 2$ for the HU and $\chi^2/\text{dof} \approx 3$ for the SR sample B. For the SR sample A, the χ^2/dof had a higher value ($\simeq 7$) due to the increased fluctuations in the experimental data. Statistical analysis of the least squares fit results of the SG window size with respect to ϑ and ϵ_ϑ is shown in the Supplementary Fig. S4. The χ^2/dof with respect to SG window and the least squares fit results with respect to the initial conditions are also shown in Supplementary Fig. S4-S5.

Acknowledgments. G.S.B. acknowledges support from the NIH award 2SC1GM086268. EF and DSN were supported by the Fellowship from Raymond and Beverly Sackler Laboratories for Convergence of Physical, Engineering and Biomedical Sciences, by the Litwin Foundation for Alzheimer’s Research, and by the NIH/NINDS award R01NS088040.

-
- [1] M. Kac, “Can one hear the shape of a drum?” *Am. Math. Mon.* **73**, 1–23 (1966).
 - [2] E. Abrahams, P. W. Anderson, D. C. Licciardello, and T. V. Ramakrishnan, “Scaling theory of localization: Absence of quantum diffusion in two dimensions,” *Phys. Rev. Lett.* **42**, 673–676 (1979).
 - [3] P. T. Callaghan, *Principles of Nuclear Magnetic Resonance Microscopy* (Clarendon, Oxford, 1991).
 - [4] R. W. Mair, G. P. Wong, D. Hoffmann, M. D. Hürlimann, S. Patz, L. M. Schwartz, and R. L. Walsworth, “Probing porous media with gas diffusion NMR,” *Phys. Rev. Lett.* **83**, 3324–3327 (1999).
 - [5] Y. Q. Song, S. Ryu, and P. N. Sen, “Determining multiple length scales in rocks,” *Nature* **406**, 178–181 (2000).
 - [6] S. Torquato, *Random heterogeneous materials: microstructure and macroscopic properties*, Vol. 16 (Springer Science & Business Media, 2013).

- [7] D. S. Novikov, E. Fieremans, J. H. Jensen, and J. A. Helpert, "Random walks with barriers," *Nat. Phys.* **7**, 508–514 (2011).
- [8] D. S. Novikov, J. H. Jensen, Joseph A. Helpert, and E. Fieremans, "Revealing mesoscopic structural universality with diffusion," *Proc. Natl. Acad. Sci.* **111**, 5088–5093 (2014).
- [9] L. M. Burcaw, E. Fieremans, and D. S. Novikov, "Mesoscopic structure of neuronal tracts from time-dependent diffusion," *NeuroImage* **114**, 18–37 (2015).
- [10] E. Fieremans, L. M. Burcaw, H. Lee, G. Lemberskiy, J. Veraart, and D. S. Novikov, "In vivo observation and biophysical interpretation of time-dependent diffusion in human white matter," *Neuroimage* **129**, 414–427 (2016).
- [11] D. K. Jones, *Diffusion MRI: Theory, Methods, and Applications* (Oxford University Press, New York, 2011).
- [12] P. C. Hohenberg and B. I. Halperin, "Theory of dynamic critical phenomena," *Rev. Mod. Phys.* **49**, 435–479 (1977).
- [13] S. Torquato and F. H. Stillinger, "Local density fluctuations, hyperuniformity, and order metrics," *Phys. Rev. E* **68**, 041113 (2003).
- [14] C. E. Zachary and S. Torquato, "Hyperuniformity in point patterns and two-phase random heterogeneous media," *J. Stat Mech-Theory E* **2009**, P12015 (2009).
- [15] C. E. Zachary, Y. Jiao, and S. Torquato, "Hyperuniform long-range correlations are a signature of disordered jammed hard-particle packings," *Phys. Rev. Lett.* **106**, 178001 (2011).
- [16] A. Aharony and A. B. Harris, "Absence of self-averaging and universal fluctuations in random systems near critical points," *Phys. Rev. Lett.* **77**, 3700–3703 (1996).
- [17] A. Gabrielli, B. Jancovici, M. Joyce, J. L. Lebowitz, L. Pietronero, and F. Sylos Labini, "Generation of primordial cosmological perturbations from statistical mechanical models," *Phys. Rev. D* **67**, 043506 (2003).
- [18] B. H. Suits and D. E. Wilken, "Improving magnetic field gradient coils for nmr imaging," *J. Phys E. Sci. Instrum.* **22**, 565 (1989).
- [19] W. Zhang and D. G. Cory, "Pulsed gradient NMR probes for solid state studies," *J. Magn. Reson.* **132**, 144–149 (1998).
- [20] M. H. Ernst, J. Machta, J. R. Dorfman, and H. van Beijeren, "Long-time tails in stationary random media. 1. Theory," *J. Stat Phys.* **34**, 477–495 (1984).
- [21] A. Savitzky and M. J. E. Golay, "Smoothing and differentiation of data by simplified least squares procedures," *Anal. Chem.* **36**, 1627–1639 (1964).
- [22] P. P. Mitra, P. N. Sen, L. M. Schwartz, and P. Le Doussal, "Diffusion propagator as a probe of the structure of porous media," *Phys. Rev. Lett.* **68**, 3555–3558 (1992).
- [23] L. L. Latour, K. Svoboda, P. P. Mitra, and C. H. Sotak, "Time-dependent diffusion of water in a biological model system," *Proc. Natl. Acad. Sci.* **91**, 1229–1233 (1994).
- [24] O. Reynaud, K. V. Winters, D. M. Hoang, Y. Z. Wadghiri, D. S. Novikov, and S. G. Kim, "Surface-to-volume ratio mapping of tumor microstructure using oscillating gradient diffusion weighted imaging," *Magn. Reson. Med.* **76**, 237–47 (2016).
- [25] P. T. Callaghan, A. Coy, D. MacGowan, K. J. Packer, and F. O. Zelaya, "Diffraction-like effects in NMR diffusion studies of fluids in porous solids," *Nature* **351**, 467–469 (1991).
- [26] F. B. Laun, T. A. Kuder, W. Semmler, and B. Stieltjes, "Determination of the defining boundary in nuclear magnetic resonance diffusion experiments," *Phys. Rev. Lett.* **107**, 048102 (2011).
- [27] M. Holz, S. R. Heil, and A. Sacco, "Temperature-dependent self-diffusion coefficients of water and six selected molecular liquids for calibration in accurate ^1H NMR PFG measurements," *Phys. Chem. Chem. Phys.* **2**, 4740–4742 (2000).
- [28] A. L. Van Geet, "Calibration of methanol nuclear magnetic resonance thermometer at low temperature," *Anal. Chem.* **42**, 679–680 (1970).
- [29] D. H. Wu, A. D. Chen, and C. S. Johnson, "An improved diffusion-ordered spectroscopy experiment incorporating bipolar-gradient pulses," *J. Magn. Reson. Ser. A* **115**, 260–264 (1995).
- [30] P. Z. Sun, J. G. Seland, and D. Cory, "Background gradient suppression in pulsed gradient stimulated echo measurements," *J. Magn. Reson.* **161**, 168–173 (2003).
- [31] P. Galvosas, F. Stallmach, and J. Kärger, "Background gradient suppression in stimulated echo NMR diffusion studies using magic pulsed field gradient ratios," *J. Magn. Reson.* **166**, 164–173 (2004).
- [32] V. G. Kiselev, "The cumulant expansion: an overarching mathematical framework for understanding diffusion nmr," *Diffusion MRI: Theory, Methods, and Applications*, 152–168 (2011).
- [33] A. Sodickson and D. G. Cory, "A generalized k-space formalism for treating the spatial aspects of a variety of NMR experiments," *Prog. Nucl. Mag. Res. Sp.* **33**, 77–108 (1998).

SUPPLEMENTARY MATERIALS

Hyperuniform sample

Fig. S1 shows a cartoon representation of the sample exhibiting hyperuniform disorder (HU). The permeable membranes had an average pore size of 45 nm, and are shown in red. The yellow parts act as a separation between the barriers to control the geometry. The thickness of the plates was $\sim (45 \pm 4) \mu\text{m}$. The parts were constructed with an open loop to minimize eddy currents.

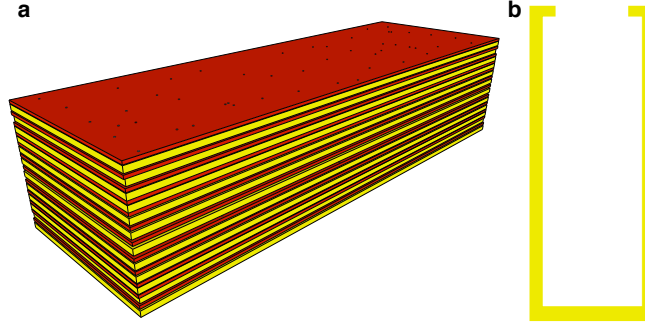


FIG. S1. Sample exhibiting hyperuniform disorder. a) Cartoon representation of the sample. The red sheets represent the permeable barriers and the yellow parts act as a separation to achieve the hyperuniformity. b) Cartoon representation of the copper plates that were inserted in the sample in order to create the layered geometry.

Diffusive permeability of a single barrier

Combining the results of Fig. 1 and 2 of the main text, we can go one step further and quantify the permeability of the barriers used to construct the samples.

Parameter $\zeta = \frac{SD_0}{2V\kappa d}$, introduced in ref. [7], is a dimensionless “barrier strength” that depends on the permeability and density of the barriers, and quantifies the ability of barriers to slow down the diffusion. The universal limit of the diffusion coefficient D_∞ , is then directly connected [7] to ζ , as $D_\infty \simeq D_0/(1 + \zeta)$. For the case of $d = 1$, which is the case in our work, the above equation is exact, and therefore determining the surface-to-volume ratio, $S/V \equiv 2/\bar{a}$ and D_∞ allows for computing the diffusive permeability κ of a single barrier. The average distance between the barriers was determined from the optical microscopy images shown in Fig. 1 of the main text (cf. Table I for values of \bar{a}). The universal limit D_∞ was determined from the long-time regime by performing least squares fit with $\text{dof} = 3$ to $D(t)$ (raw data shown in Fig. S3).

For the SR sample created with barriers having an average pore diameter of 15 nm (sample A in Fig. 1 of the main text), $D_\infty|_{15\text{nm}} = (0.42 \pm 0.04) \mu\text{m}^2/\text{ms}$, $\zeta|_{15\text{nm}} \simeq 4.6$ resulting in $\kappa|_{15\text{nm}} = (0.04 \pm 0.01) \mu\text{m}/\text{ms}$. For the SR sample created with barriers having an average pore diameter of 45 nm (sample B in Fig. 1 of the main text), $D_\infty|_{45\text{nm}} = (0.58 \pm 0.05) \mu\text{m}^2/\text{ms}$, $\zeta|_{45\text{nm}} \simeq 2.7$ resulting in $\kappa|_{45\text{nm}} = (0.06 \pm 0.02) \mu\text{m}/\text{ms}$. Note that for the sample exhibiting hyperuniform disorder, the spacers used for controlling the geometry will artificially lower D_∞ resulting a lower diffusive permeability κ . It is therefore more accurate to determine the permeability of the barriers using the diffusion coefficient from the samples exhibiting short-range disorder.

Diffusion NMR methodology

Fig. S2 highlights the pulse sequences used in this work.

The time interval Ξ was varied for each experiment from approximately 50 μs to 4.5 s. The gradient pulse width was $\delta = 120 \mu\text{s}$ for diffusion times of 1 ms to 1.3 ms and $\delta = 240 \mu\text{s}$ for diffusion times of 1.4 ms to 4.5 s. The $\pi/2$ pulse had a duration of $pw = 5 \mu\text{s}$ and the π a duration of 10 μs . The delay τ was 50 μs for the pulse sequence for short times and 500 μs for the pulse sequence for long times. The crushing gradient δ_c had a duration of 150 μs and is used to spatially encode any single quantum coherence left after the $\pi/2$ pulse. The time interval T between the $\pi/2$ pulses was 2 ms and is used to push the echo further in time to mitigate ring down effects. The total diffusion time reported in Fig. 2-3 includes the time intervals that the molecules acquire the phase $e^{i\phi}$ due to the gradients and is given by $t = 4(\delta + \tau + pw) + \Xi$.

The short-time regime

The pulse sequence used for diffusion times between 1 to 50 ms is shown in Fig. S2a [29]. The use of bipolar gradients compensate for the eddy currents induced by the fast changing current. It should be noted here that the background gradient g_0 was estimated based on the measured line width, $f = 350$ Hz, and sample size of $L \simeq 1$ mm, and found to be $g_0 \simeq 0.8$ G/cm. Therefore the background gradients are not expected to introduce any artificial fluctuations in the measured diffusion coefficient at short times.

The shaped gradient pulses alternate the form of b given in ref. [29]. The spatial wavenumber is given by $q(t) = \int_0^t dt' g(t')$ where $g(t)$ is the gradient waveform with respect to time. The attenuation of magnetization due to the the gradients is given by $-D_0 \int_0^t dt' q^2(t')$ [32, 33]. For the pulse sequence shown in Fig. S2a the signal attenuation is given by,

$$S(g_m) = -D_0 \left(16g_m^2 \tau \gamma^2 \delta^2 + 22g_m^2 \gamma^2 \delta^3 + 16g_m^2 \gamma^2 \delta^2 \Xi \right) \frac{1}{\pi^2}. \quad (4)$$

In eq. (4), g_m is the maximum gradient strength and γ is the ^1H gyromagnetic ratio. Note that the term proportional to Ξ will dominate for $\Xi > 8$ ms. The phase cycling used for the short-time measurements is provided in ref. [29].

The long-time regime

The pulse sequence used for diffusion times between 50 ms to 4.5 s is shown in Fig. S2b [30, 31]. The signal attenuation for the pulse sequence shown in S2b is given by,

$$\begin{aligned} S(g_m) = -D_0 \left((g_0^2 + g_0'^2) \left[\frac{2\tau^3 \gamma^2}{3} + 2\tau^2 \gamma^2 \delta \right. \right. \\ \left. \left. + 2\tau \gamma^2 \delta^2 + \frac{2\gamma^2 \delta^3}{3} \right] + [-2g_{m2} \gamma \delta - 2g_{m2} \gamma \delta \eta]^2 \frac{\Xi}{\pi^2} + \right. \\ \left. [3\gamma^2 \delta^3 + 8\gamma^2 \delta^3 \eta + 16\tau \gamma^2 \eta^2 + 11\gamma^2 \delta^3 \eta^2] \frac{g_{m2}^2}{\pi^2} \right), \end{aligned} \quad (5)$$

with,

$$\eta = -\frac{\delta^2(-4 + \pi^2)}{\pi^2(4\tau^2 + 8\tau\delta + \frac{4\delta^2}{\pi^2} + 3\delta^2)}. \quad (6)$$

In the above equation g_0 and g_0' are the values of the background gradients during the encoding and decoding time intervals and were estimated to be approximately 0.8-1 G/cm based on the linewidth. The ratio $\eta = g_{m2}/g_{m1}$ is defined by eq. (6); choosing an appropriate η suppresses the $g_0 g_m$ term in the signal attenuation. Note that the term proportional to Ξ dominates for $\Xi > 20$ ms. The phase cycling for long-time measurements is provided in ref. [30].

Statistics of the least squares fitting procedures

Cumulative diffusion coefficient (D)

A least squares power law fitting procedure with three degrees of freedom was used to estimate the dynamical exponent $\tilde{\vartheta}$, the universal diffusion coefficient at long times D_∞ , and the coefficient c according to,

$$D(t) = D_\infty + ct^{-\tilde{\vartheta}}. \quad (7)$$

The results are shown as solid lines in Fig. S3 and the χ^2/dof for all three fitting procedures was approximately 0.8. The resulting $\tilde{\vartheta}$ from the least squares fitting procedure is shown in Table I of the main text.

Instantaneous diffusion coefficient (D_{inst})

Figure S4 shows the statistics of SG window size and polynomial order for the χ^2/dof and $\vartheta \pm \epsilon_\vartheta$ for the sample exhibiting hyperuniform disorder. The statistics for different SG window size (as percentage) are shown in Fig. S5a. A two degrees of freedom least squares fit was used for ϑ and c by using the D_∞ value from the cumulative diffusion coefficient fit. The resulting ϑ was observed to converge to the expected theoretical values as the SG window is increased. The computed χ^2/dof is shown to decrease with respect to the SG window and plateaus to a reasonable value ($\simeq 3$) for short-range disorder (Sample B), and hyperuniform disorder ($\simeq 2$) (Sample C). On the other hand, for the other sample exhibiting short-range disorder (Sample A) the χ^2/dof had a higher value ($\simeq 7$) due to increased fluctuations in the experimental data. The results of the least squares fit procedure for ϑ with respect to the initial conditions are shown in Fig. S5b-c-d and show a reasonable Gaussian shape with a tail for the samples A-B (green-blue) and a bimodal distribution for C (red).

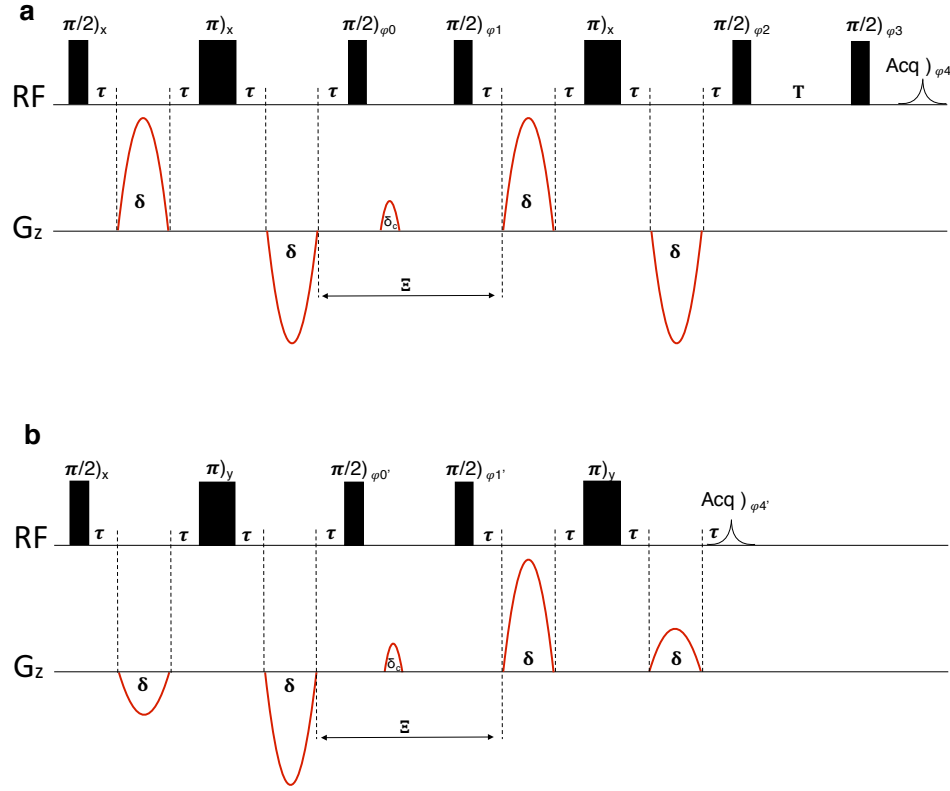


FIG. S2. NMR pulse sequences used in this work. Shaped pulses were used to mitigate ringdown effects which introduce imperfections in the gradient pulses and result in errors in the k-space trajectories [33]. In addition, the π pulses refocus evolution under the background gradients colinear with the Zeeman field at time 4τ . a) NMR pulse sequence used for measuring diffusion for times between 1 to 50 ms [29]. The use of bipolar magnetic field gradient pulses compensate for eddy currents. The phases of the RF pulses for this pulse sequence are given in ref. [29]. b) NMR pulse sequence used for measuring diffusion for times between 50 ms to 4.5 s [30, 31]. The use of assymmetric magnetic field gradient pulses cancels the cross term between the applied magnetic field gradient g and the background gradient, g_b , after decoding. The phases of the RF pulses for this pulse sequence are given in ref. [30].

Surface-to-volume ratio (S/V)

Fig. S6 highlights statistics of one and two degrees of freedom least squares fit results (\bar{a} and D_0), with respect to the dimensionless ratio t/τ_D . Each point in Fig. S6 represents the first point of a least squares fit with a time range varying from $0.05\tau_D$ for $t \ll \tau_D$ to $\tau_D/2$ for $t \simeq \tau_D$. Note that the increments of time δt where always much smaller than the window of the fit. Therefore the results of Fig. S6 correspond to local slopes along $D(t)$ in Fig. 3. Fig. S6a-b shows the fit results of the mean barrier spacing \bar{a} and free diffusion coefficient D_0 along with the known values (black lines). It is evident that the fit results agree with the predictions for $t/\tau_D < 0.1$ suggesting that the fitted S/V will be substantially underestimated if not at this time regime. Fig. S6c highlights the fitted \bar{a} by fixing D_0 to the theoretical value at the corresponding temperature ($D_0 = 2.30 \mu\text{m}^2/\text{ms}$ at 25°C).

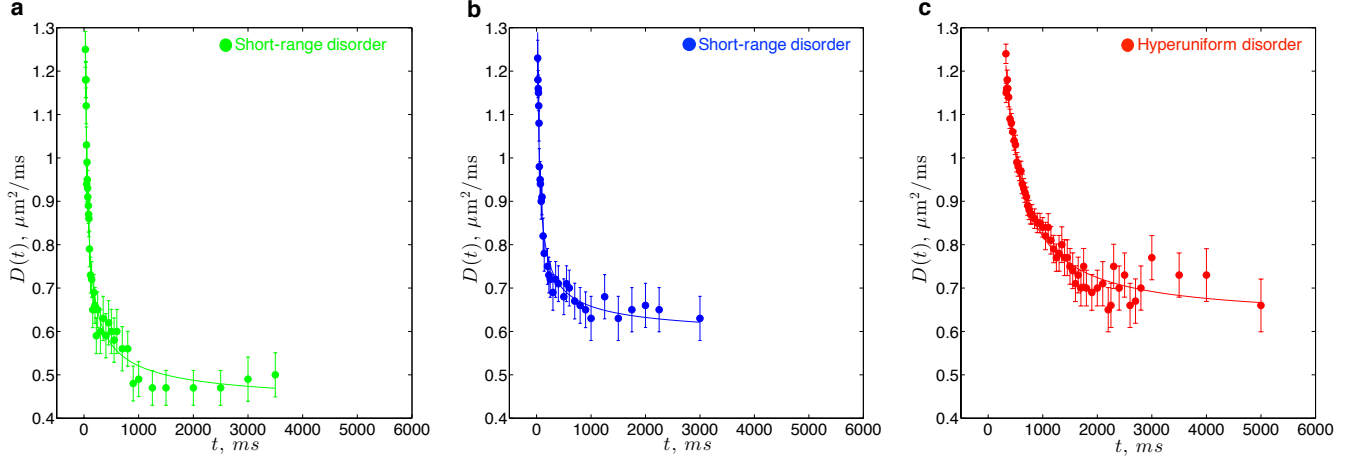


FIG. S3. Measured diffusion coefficient with respect to the diffusion time for the three disordered samples used in this work. The solid line corresponds to a least squares fit with three degrees of freedom to eq. (7).

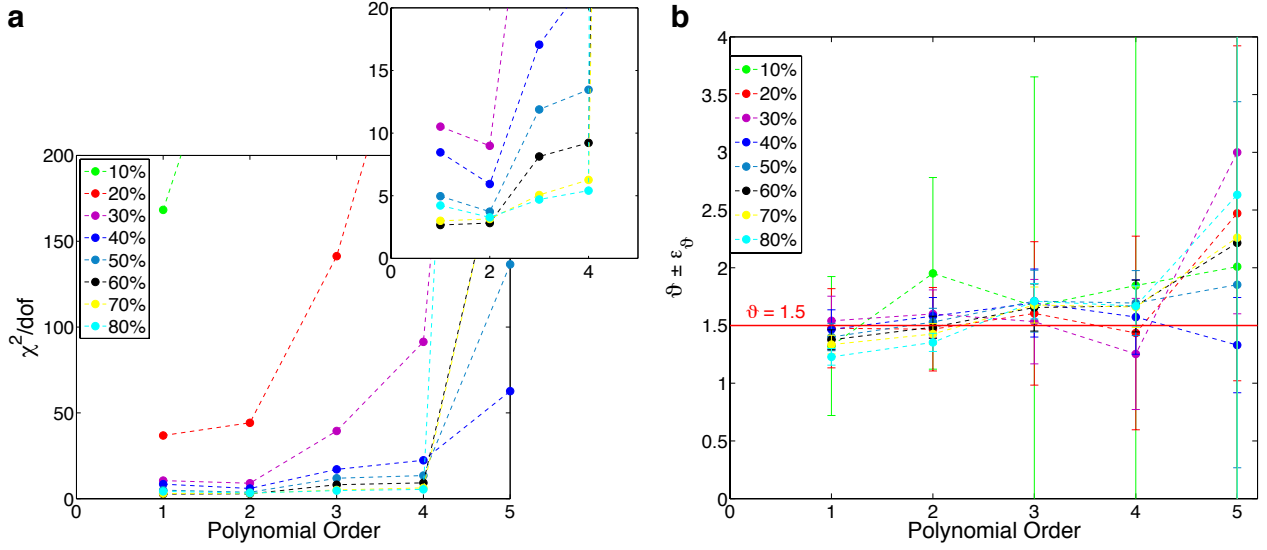


FIG. S4. Statistics of the Savitzky-Golay smoothing procedure (percentage) with respect to the polynomial order for the sample exhibiting hyperuniform disorder (C-red). a) χ^2/dof diverges as the polynomial order is increased. b) Least squares power law fit with two degrees of freedom reveals that the fitted value for ϑ converges to the expected power law for low polynomial order and converges for high polynomial order.

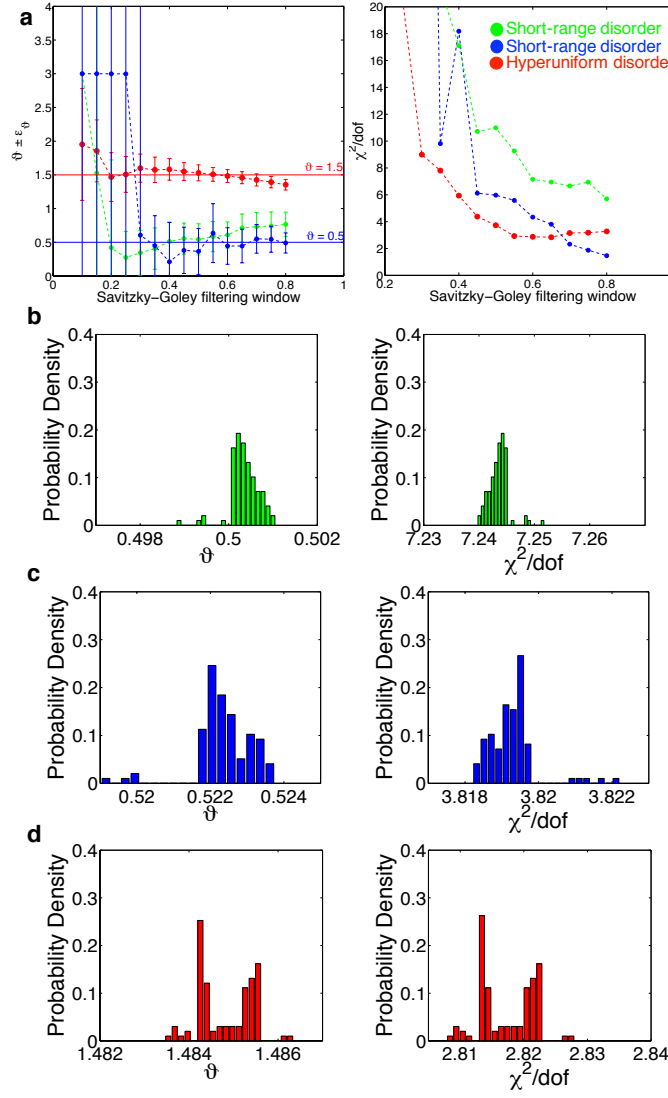


FIG. S5. Statistics of the Savitzky-Golay smoothing procedure and least squares power law fit with two degrees of freedom. a) Resulting power law least squares fit and error, $\vartheta \pm \epsilon_\vartheta$, with respect to Savitzky-Golay filtering window of the three disorder classes. As discussed in the text, increasing the filtering window reduces the noise, and thus the error, revealing the true exponent ϑ . Reduced χ^2 with respect to Savitzky-Golay filtering window of the three disorder classes. The chosen dynamic window for the three data sets was ± 0.6 (60%) of the central time point of the window. b-c-d) Statistics for the power law fit and reduced χ^2 of the filtered D_{inst} for the three disorder classes for multiple initial conditions. The resulting least squares fit parameters, ϑ and c (not shown) were robust for short-range disorder (blue) and hyperuniform disorder (red) as shown from the reduced χ^2 distribution. The resulting least squares fit parameters for short-range (green) don't show large deviation with respect to the initial conditions but the reduced χ^2 is high due to the increased scatter in the data.

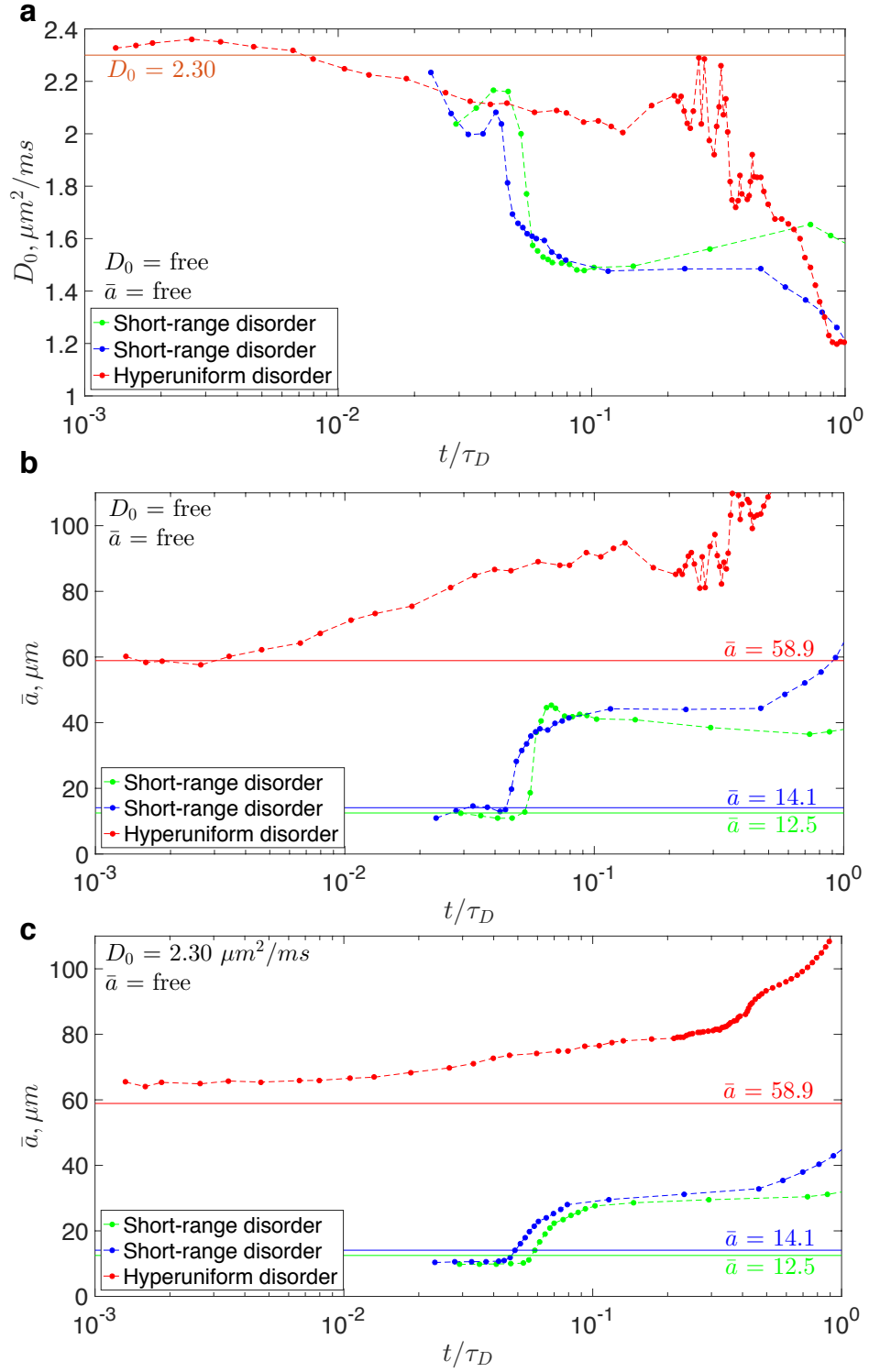


FIG. S6. Statistics of the surface-to-volume ratio least squares fitting procedure with two (a-b) and one (c) degrees of freedom with respect to the fit window with a dynamic range. Each point represents the first point of the fit. a) Fitted \bar{a} ; b) D_0 ; c) \bar{a} with respect to the fit window using a fixed $D_0 = 2.30 \mu\text{m}^2/\text{ms}$.